Technical note: Quantification of ultrafine particle mass deposition in an *in vitro* air-liquid interface exposure system

Anusmita Das [a,b], Mathilde Noemie Delaval [a], Mika Ihalainen [c], Jürgen Schnelle-Kreis [a], Anja Huber [a,b], Elias J. Zimmermann [a,b], Sebastiano Di Bucchianico [a,b,d], Olli Sippula [c,e], Hendryk Czech [a,b,*] , Martin Sklorz [a,b], Ralf Zimmermann [a,b,d]

[a] *Joint Mass Spectrometry Center (JMSC) at Comprehensive Molecular Analytics (CMA), Helmholtz Zentrum München, Ingolstädter Landstrasse 1, Neuherberg, D-85764, Germany*
[b] *Joint Mass Spectrometry Center (JMSC) at Chair of Analytical Chemistry, Institute of Chemistry, University of Rostock, Albert-Einstein-Strasse 27, D-18059, Rostock, Germany*
[c] *Department of Environmental and Biological Sciences, University of Eastern Finland, 70211, Kuopio, Finland*
[d] *Department Life, Light & Matter, University of Rostock, Albert-Einstein-Strasse 25, D-18059, Rostock, Germany*
[e] *Department of Chemistry, University of Eastern Finland, 80101, Joensuu, Finland*

ARTICLE INFO

ABSTRACT

Air-Liquid Interface (ALI) cell exposure systems are essential tools for assessing the toxicity of airborne aerosols and engineered nanomaterials *in vitro*. These systems are increasingly favored for depositing aerosols directly onto cell cultures with improved precision, scalability, and flexibility. However, a significant challenge remains in accurately determining the actual particle deposition, particularly for ultrafine particles (UFP, Dp ≤ 100 nm). This study investigates the chemical-based quantification of UFP mass deposition and the deposition variability across insert positions in an Automated Exposure Station (AES).

Multi-well positions in the AES were exposed to soot UFP, rich in polycyclic aromatic hydrocarbons (PAH), and copper UFP for 4 h in independent experiments. To determine the mass deposition of soot UFP, Teflon-coated glass fiber filters were placed at various positions and analyzed to quantify targeted PAH. Similarly, copper UFP was deposited onto empty inserts in different positions, and post-exposure quantification was performed.

Mass deposition efficiencies exhibited a high relative variability of 15 % from experiment to experiment, and the position-dependent variability was not significant for either soot UFP or copper UFP. However, compared to the results from a theoretical model, the model significantly underestimated mass deposition by a factor of 5–8. Incorporating an alternative calculation of the boundary layer thickness into the model improved the agreement between model and experimental data. Therefore, for UFP mass deposition results from modeling must be interpreted with care.

* Corresponding author. Joint Mass Spectrometry Center (JMSC) at Chair of Analytical Chemistry, Institute of Chemistry, University of Rostock, Albert-Einstein-Strasse 27, D-18059 Rostock, Germany.
E-mail address: hendryk.czech@uni-rostock.de (H. Czech).

1. Introduction

Ultrafine particles (UFP; Particulate matter ($PM_{0.1}$)) are particles with an aerodynamic diameter smaller than 0.1 μm, which may originate from both natural and human activities. Natural sources include volcanic eruptions, wildfires, sea spray and the formation of secondary organic aerosol by oxidation and condensation of e.g. biogenic volatile components, while anthropogenic emissions primarily result from combustion-related processes such as transportation, industrial activities, power generation, waste incineration, cigarette smoke, and biomass burning (Hofmann, 2011; Kwon et al., 2020; Schraufnagel, 2020). Meanwhile, the contribution of UFP to the atmosphere from anthropogenic non-combustion processes originating from brake pads, tire abrasions, friction between wheels and roads/rails, or catenary sparking is gaining more attention (Font et al., 2019; Fussell et al., 2022; Neukirchen et al., 2025). The current knowledge about the effects of UFP on health comes from toxicological and epidemiological research. Epidemiological research highlights the potential risks associated with UFP exposure (Folwarczny et al., 2025; Ohlwein et al., 2019; Schwarz et al., 2023). Epidemiological studies are essential for evaluating human exposure in realistic settings; however, they often struggle to estimate actual exposure levels accurately (Folwarczny et al., 2025). These studies typically rely on sparse measurements taken at monitoring sites distant from the affected populations or use modeling approaches with inherent assumptions (Vallabani et al., 2023). Hence, providing precise measurements of exposure concentration and duration, toxicological studies are essential.

UFP has been associated both *in vivo* and *in vitro* with various harmful effects due to its capacity to induce oxidative stress, inflammation, and genotoxicity (Moreno-Ríos et al., 2022; Vallabani et al., 2023). Compared to larger particulate matter, UFP can translocate from the lung into various secondary target organs by crossing the air-blood barrier or penetrating the blood-brain barrier and subsequently inducing extra-pulmonary effects. Moreover, UFP possess a large surface area to mass ratio, enabling them to adsorb significant quantities of toxic compounds (Kwon et al., 2020). This intrinsic property of UFP accounts for an essential portion of the total particle number concentration in urban areas. While current studies have made substantial progress in elucidating the biological effects and mechanisms of action of UFP, recent literature highlights the ongoing need for advanced experimental and computational approaches to investigate UFP deposition dynamics, as well as the development of appropriate metrics for evaluating associated health risks.

Toxicological research on UFP-related health effects increasingly relies on a combination of *in vivo* and *in vitro* exposure models to capture both systemic and cellular responses. Air-liquid interface (ALI) cell exposure systems are increasingly prevalent in *in vitro* studies over submersed exposure conditions for a more realistic exposure, where solid or liquid particles are typically mixed with surrounding gases and directly applied to tissue-cell cultures (Paur et al., 2011; Thorne & Adamson, 2013). Studies investigating the toxicity of UFP using ALI exposure systems have been emerging, such as for high aromatic and non-aromatic diesel fuel exhaust emissions (Hakkarainen et al., 2023), aircraft engine emissions (Delaval et al., 2022; Jonsdottir et al., 2019), printer emissions (Kim et al., 2022), model UFP from miniCAST generators taking into account similar physical and different chemical UFP properties (Das et al., 2024; Juarez Facio et al., 2022; Offer et al., 2022). In these studies, particle deposition onto the cell layer was primarily estimated using model calculations based on measured aerosol properties. This is usually done for simplicity, and measurements of mass-based deposition for UFP in the ALI are challenging. However, these models can be used for particles ranging from 40 to 450 nm; the ALI-deposited mass estimated with computational models was found to be 1-2 orders of magnitude greater than in the alveolar region of the lungs due to the ALI's smaller surface area (Karg et al., 2020). These findings underscore the need for careful interpretation when extrapolating *in vitro* ALI exposure results to *in vivo* lung exposures.

Studies on aerosol particle dosimetry at the ALI typically utilize inert solid particles that are fluorescently tagged with glycerol (Bannuscher et al., 2022; Steiner et al., 2017), e-cigarette vapor products (Adamson et al., 2016; Neilson et al., 2015), and mainstream tobacco smoke (Adamson et al., 2013; Aufderheide et al., 2017). Inert solid particles have also been extensively employed to develop computational models within these *in vitro* exposure systems (Comouth et al., 2013; Fujitani et al., 2015; Kim et al., 2013; Lucci et al., 2018; Oldham et al., 2020; Tippe et al., 2002). In the first study aiming to characterize the deposited dose in a VITROCELL® exposure system experimentally, Mülhopt et al. (2016) determined the deposition efficiency of wood combustion UFP by analyzing deposited particles on TEM grids. They showed a good agreement within the diffusional deposition compared to estimated deposited dose based on the particle number and size distribution from SMPS. However, no studies have examined the deposition of combustion-derived UFP in aerosol exposure systems by quantifying chemical components of the UFP, which would allow for the elimination of uncertainties introduced by the size-dependent particle density and their inherent physical properties. Due to their small size, UFP deposition is primarily governed by diffusion processes, making it challenging to quantify the dose deposited onto cells in experimental setups accurately. As ALI exposure systems continue to grow in complexity, a thorough understanding of their capabilities, operational conditions, and reproducibility is essential to ensure reliable and biologically relevant results (Lucci et al., 2018). Our study aims to fill this gap on deposition uncertainty for UFP by experimentally determining depositions for soot and copper UFP, comparison to common theoretical deposition models and discussing model appropriate for deposition determination in ALI systems.

2. Materials and methods

2.1. UFP production

Two ultrafine particles (UFP) types were generated using different aerosol generators. Soot UFP with a high organic load (Soot-UFP), was produced using a miniCAST soot generator (miniCAST, model 5201C; Jing Ltd., Switzerland) following the method described by Das et al. (2024). The second type, copper UFP (Cu-UFP), was generated using a Spark Discharge Generator (SDG, model GFG 1000; Palas, Germany) equipped with cylindrical copper electrodes. All exposure experiments were conducted over 4 h, matching

the duration used for previous *in vitro* studies in our group (Binder et al., 2022; Das et al., 2024; Offer et al., 2022; Pardo et al., 2023). Conductive perfluoroalkoxy (PFA) tubing was used in both setups to minimize particle losses and reactions. This material prevents static electric charge accumulation, which can cause particle losses, offering high transmission efficiency (Liu et al., 2019). Depending on the flow rates, PFA tubes with inner diameters of 4 mm or 10 mm were used to minimize losses due to turbulence and ensure laminar flow.

2.1.1. Soot UFP (Soot-UFP)

The miniature combustion aerosol standard soot generator (miniCAST, model 5201C; Jing Ltd., Switzerland) was operated under fuel-rich conditions (flame equivalence ratio, $\Phi = 1.25$) to produce soot UFP with a high organic content. A critical parameter characterizing the miniCAST operating regime is the overall fuel-to-air ratio, commonly expressed as the flame equivalence ratio (Φ). The generator operates in a fuel-rich mode when $\Phi > 1$, whereas fuel-lean or near-stoichiometric conditions correspond to $\Phi < 1$. In this study, the operating flow rates were set as follows: propane at 0.055 L min^{-1}, dilution air at 20 L min^{-1}, burner air at 1.05 L min^{-1}, and quench nitrogen (N$_2$) at 7 L min^{-1}. The primary soot particles were immediately diluted to minimize agglomerations through an in-house-built adjustable porous tube diluter (PTD) and fixed 10-fold ejector diluters (VKL 10; Palas, Germany). The dilution in the PTD was adjusted at the beginning of each experiment and then readjusted periodically over the 4 h to maintain constant particle number and mass concentrations throughout the experiment. A catalytic stripper (CS, Model CS015; Catalytic Instruments, Germany) was used at room temperature, followed by a multichannel activated charcoal denuder, to achieve particle physical characteristics similar to those observed by Das et al. (2024). Following the denuder, a second 1:10 ejector diluter was used for an additional dilution step, maintaining a constant flow rate of 1.65 L min^{-1}. Subsequently, the Soot-UFP was directed to the VITROCELL ® Automated Exposure Station extended version (AES, VITROCELL GmbH, Germany), where it was collected for offline analysis and characterized using various instruments for real-time characterization of the UFP. Fig. 1 presents a schematic of the experimental setup for Soot-UFP.

2.1.2. Copper UFP (Cu-UFP)

Fig. 2 shows a schematic view of the experimental setup for the Cu-UFP. A spark discharge generator (SDG, Palas GFG 1000, Germany) was operated at a volumetric flow rate of approximately 4.75 L min^{-1} of pure argon (Ar) (99.999 %, Linde, Germany) and a spark frequency of 800–999 Hz, using copper electrodes positioned 2 mm apart. The Cu-UFP was subsequently neutralized using a Palas neutralizer (model XRC 049), then passed through a 5 L vessel and a 3 m long perfluoroalkoxy (PFA) coil with an internal diameter of 10 mm to obtain the desired particle mobility diameter (similar to Soot-UFP) through agglomeration. The Cu-UFP was then guided through a square, multi-channelled charcoal denuder with 325 square channels, each measuring 0.9 mm × 0.9 mm (Helsatech, Germany), to remove gas-phase organics potentially originating from the vessel (Binder et al., 2022; Das et al., 2024). The Cu-UFP was then diluted using an ejector diluter with a fixed 1:10 dilution ratio (VKL 10; Palas, Germany) to achieve the desired particle number
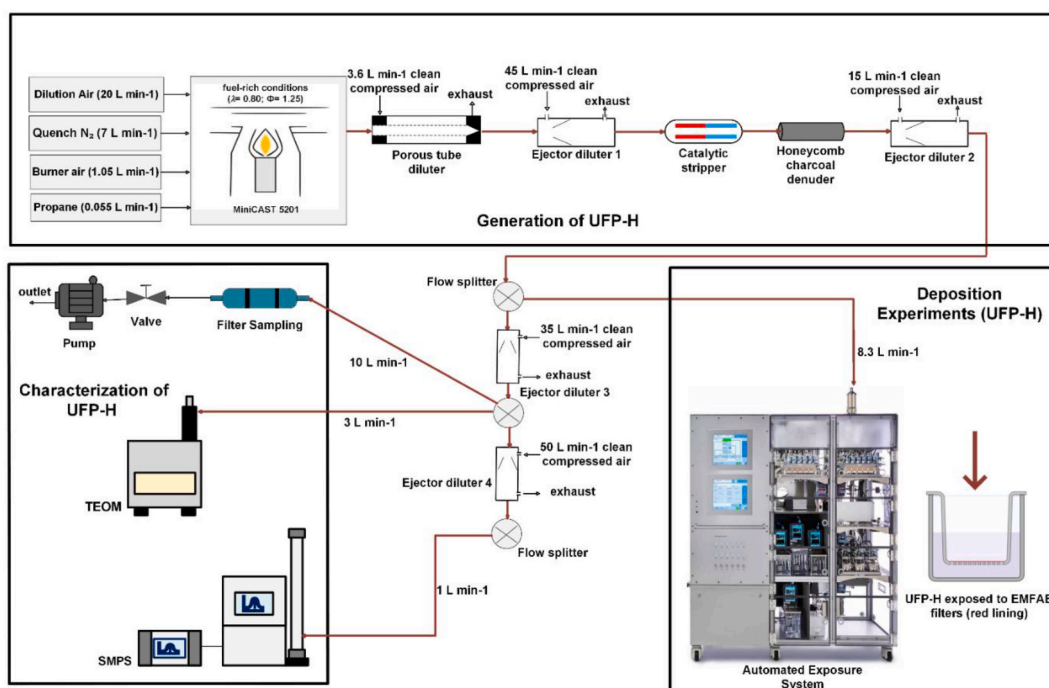

Fig. 1. Schematic diagram of the setup used to produce soot ultrafine particles with a high organic load (Soot-UFP). The setup includes a Tapered Element Oscillating Microbalance (TEOM) for measuring mass concentration and a Scanning Mobility Particle Sizer (SMPS) for analysing particle size distribution.
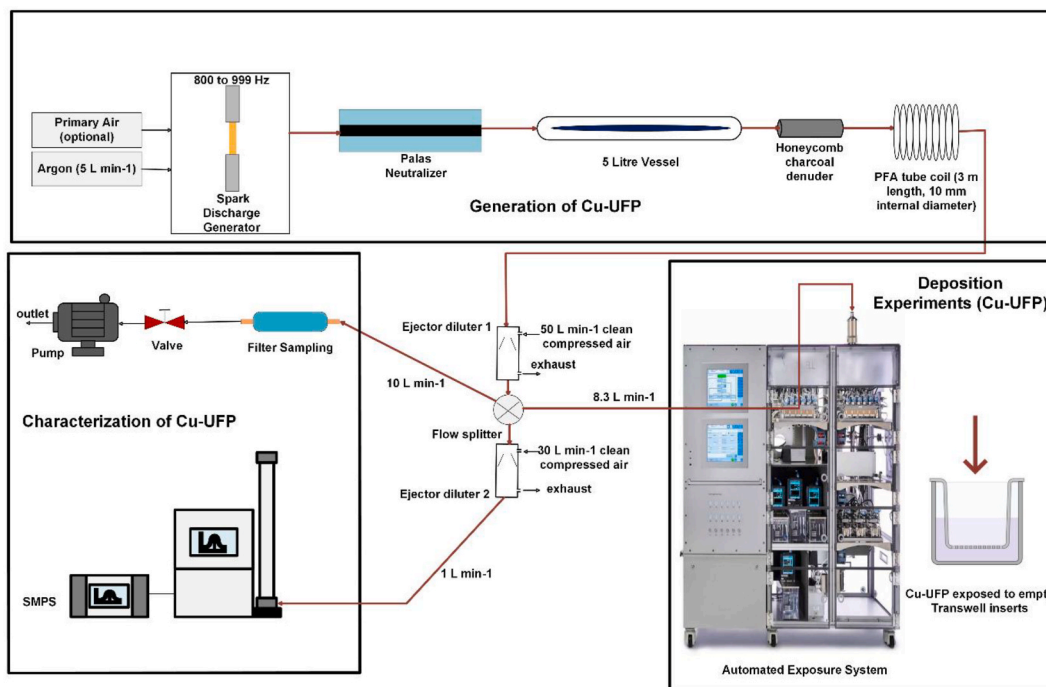
Fig. 2. Schematic diagram of the setup used for producing copper ultrafine particles (Cu-UFP). The particle size distribution was measured using a Scanning Mobility Particle Sizer (SMPS).

concentration. The diluted Cu-UFP was then distributed to the VITROCELL® AES for the deposition studies, collected on filters for offline analysis, or further diluted (1:10 ratio) for online characterization.

2.2. UFP online characterization

A Scanning Mobility Particle Sizer (SMPS, Type 3082, TSI Incorporated, USA) was used to determine the size distribution, particle number concentration, and the geometric mobility diameter (GMD_{mob}). The size range for SMPS analysis was 7.64–310.6 nm, with a sheath flow of 10 L min^{-1} and an aerosol flow of 1 L min^{-1}. A Tapered-Element Oscillating Microbalance (TEOM 1400a; Rupprecht & Patashnick Co., Inc., USA) was used to determine the particle mass concentration of Soot-UFP operating at a total flow rate of 3 L min^{-1}, similar to the parameters used by Das et al. (2024).

2.3. UFP offline characterization

Quartz fiber filters (QFF, Whatman, Cytiva Ltd., USA) were used to collect the UFP filter samples. Before use, these filters were preheated for 5 h at 550 °C. Targeted quantification of Polycyclic Aromatic Hydrocarbons (PAH) was carried out using Gas Chromatography-Mass Spectrometry (GC-MS, Shimadzu GC-MS-QP2010 Ultra, DTD-20 Shimadzu, Japan) operated in Single Ion Monitoring (SIM) mode. The sample introduction into the instrument was done by direct thermal desorption (DTD) with the OPTIC-4 inlet (GL Sciences B.V., The Netherlands) (Orasche et al., 2011). Further details of the analytical procedure can be found in Schnelle-Kreis et al. (2005). The targeted quantification was done for three particle-bound PAH (≥5 aromatic rings), namely Benzo-fluoranthenes [sum of b + j + k isomers], Benzo[e]pyrene and Benzo[a]pyrene using the SIM mode. Each sample was measured at least twice as common practice for quality control and stored at −20 °C until the analysis.

The copper content in filter samples was quantified using an Atomic Absorption Spectrometer (AAS ZEEnit 600s; Analytik Jena, Germany) equipped with Zeeman correction and a graphite furnace atomizer. A hollow cathode lamp (copper type) was used, with method parameters set in the instrument software: an analytical wavelength of 324.8 nm, a spectral bandpass of 0.5 nm, and a lamp current of 2 mA. Calibration was performed using a certified copper AAS standard solution (ROTI®Star, 1000 mg L^{-1} Cu in 2 % HNO$_3$) at concentrations of 2, 5, 10, 15, and 20 µg L^{-1}. A 10 % HNO$_3$ solution served as a blank, followed by a 10 µg L^{-1} control standard (Analytik Jena, copper AAS standard, 2 mg L^{-1} in 0.2 % HNO$_3$), prepared by diluting 0.125 mL of the 2 ppm solution in 25 mL. The calibration curve was established with a 95.4 % confidence interval to ensure reliable quantification of copper.

For copper extraction, the quartz fiber filters (QFFs) were treated with 10 mL of 10 % HNO$_3$ (ROTIPURAN® Supra, 69 %). The samples were centrifuged at 3000 rpm for 5 min to separate particulates, and the supernatant was filtered through a 0.45 µm nylon filter to remove residual debris. A 1:200 pre-dilution was performed before the AAS measurement to bring the copper concentration within the calibration range. Eppendorf pipettes and corresponding tips were used for all liquid handling to ensure precision and

accuracy. Each sample was measured at least twice to verify reproducibility in quantifying copper concentrations. Samples were stored in a silica desiccator until analysis.

2.4. Deposition experiments

For the deposition study, 24 mm Transwell® 0.4 μm pore-size polyester membrane inserts (#3450, Corning, NY, USA) were exposed at the air-liquid interface (ALI) to UFP using the Vitrocell® AES. The system was operated as previously described (Mülhopt, 2016), with settings similar to those in Offer et al. (2022) and Pantzke et al. (2023). UPF-H and Cu-UPF aerosols were conducted to the AES as shown in Figs. 1 and 2, and the total aerosol flow incoming to the system was 8.3 L min^{-1} (500 L h^{-1}). The aerosols were further conditioned to 85 % relative humidity (RH) and 37 °C and directed at a flow rate of 100 mL min^{-1} to the inserts placed in individual exposure units inside the exposure modules. Two aerosol modules (defined as X and Y), comprising six exposure units each, were used in this study. An additional dedicated exposure module with six exposure units served as clean air (CA) control (100 mL min^{-1} of clean air humidified to 85 % RH at 37 °C, per exposure unit). The AES was routinely operated during the 4 h exposure to maintain the inserts under stable temperature and relative humidity.

Prior to a series of experiments, the height of each trumpet inlet was adjusted at 2 mm from the collection point with the distance sensor. Each exposure lasted for 240 min and was repeated accordingly for different experiments. During exposure, RH and temperature were recorded at the insert level in both the exposure and clean air modules with additional sensors, as previously described (Zimmermann et al., 2025). The measured values were within the acceptable range for cell exposure (85 % ± 5 % r.H, 37 °C ± 0.5 °C).

2.4.1. Quantifying mass deposition

2.4.1.1. Soot UFP (Soot-UFP).
Emfab air monitoring filters (TX40HI20WW, 47 mm; Pall Corporation, NY, USA) were cut to fit into Transwell inserts for collecting UFP during exposure. The EMFAB filters were exposed to UFP in ten exposure units, divided into two aerosol modules: four exposure units in Module X (X1, X2, X3, X5) and six exposure units in Module Y (Y1, Y2, Y3, Y4, Y5, Y6). For the Soot-UFP experiments, unit X4 was unavailable as this position was used for a different study. The media reservoir beneath the Transwell was filled with deionized water instead of culture media, following the method described by Oldham et al. (2020). After exposure, the filters were collected and stored at −20 °C until analysis. For analysis, each filter was halved, and both halves were analyzed separately using TD-GCMS. Each half was carefully rolled and placed in the GC injection liner to prevent obstruction of carrier flow. Thermal desorption was conducted at 260 °C. Three particle-associated PAH with ≥5 aromatic rings were targeted and quantified to use them as markers for the Soot-UFP. The marker PAH, Benzofluoranthenes [sum of b + j + k isomers], Benzo[e]pyrene and Benzo[a]pyrene were then measured in SIM mode using DTD-GC MS.

2.4.1.2. Copper-UFP (Cu-UFP).
Empty Transwell® inserts were placed in the exposure modules for 4 h of exposure with deionized water in place of media beneath. For quantifying the deposition of Cu-UFP in nine exposure units in two aerosol modules, with four exposure units in module X (X1, X2, X3, X4) and five exposure units in the aerosol module Y (Y1, Y2, Y3, Y5, Y6). For the Cu-UFP experiments, units X5 and Y4 were unavailable, as these positions were used for a different study. After the exposure, the Transwell® membranes were cut, collected, and stored in a silica desiccator until analysis. The membranes were then extracted for copper analysis. They were treated with 1 mL of 10 % HNO$_3$ (ROTIPURAN® Supra, 69 %) and vortexed for 2 min at 3000 rpm. A 1:20 predilution was performed before the AAS measurement to bring the copper concentration within the calibration range. The copper was then quantified from the inserts with the AAS.

2.4.2. Theoretical analyses of UFP mass deposition
The AES's deposited particle mass per area was calculated using equation (1):

$$Deposited\ mass\ per\ area = \frac{\eta \times Q \times N \times t \times \rho_p \times V_p}{A} \qquad \text{Equation 1}$$

where η is the deposition efficiency; Q is the aerosol flow; N is the particle number concentration (particle count per volume); t is the duration of the exposure; ρ_p is the particle density; V_p is the particle volume, assuming spherical particles; and A is the area of the insert. The size-dependent deposition efficiency (η) in the ALI exposure system was calculated using the theoretical framework used by (Lucci et al., 2018). Diffusion and sedimentation mechanisms within the model govern the deposition of particles. Diffusion is the dominant mechanism for the deposition of small particles, while gravitational settling or sedimentation is the dominant mechanism for larger particles. The deposition efficiency in the model by Lucci et al. (2018) is calculated using equation (2).

$$\eta_i = min\left\{1, \frac{A}{q_v}\left(v_{s,i} + \frac{D_i}{\delta_i}\right)\right\} \qquad \text{Equation 2}$$

where η_i is the size-dependent deposition efficiency; A is the area of the insert/deposition plate; q_v is the sampling flow rate; $v_{s,i}$ is the settling velocity; D_i is the aerosol size-dependent coefficient of diffusion; and δ_i is the aerosol size-dependent boundary layer thickness. The δ_i in equation (2) was calculated using equation (3).

$$\delta_i^H = \left(\frac{D_i}{\nu}\right)^{1/3} \sqrt{\frac{\nu x}{u}}$$

Equation 3

Where δ_i^H is the estimate of the aerosol thickness; x is 2/3 R (radius of the insert/deposition plate); and u is the reference velocity inside the trumpet.

Another approach to evaluate the δ_i is to model it as the root-mean-square of the particle Brownian displacement during a characteristic time t_c, as described by (Hinds., 1999) as shown in equation (4). This approach was selected because the particles in our experiments were small, necessitating that we modify the model to take into consideration variations in the equation's diffusion component.

$$\delta_i^B = \sqrt{(2D_i t_c)}$$

Equation 4

Where the characteristic time, t_c, is defined as the ratio between the chamber volume and the sampling rate (Grabinski et al., 2015).

We compared the results obtained from Equations (3) and (4), focusing on diffusion as the primary deposition mechanism, to determine which equation is more appropriate for the system investigated in this study, with the mobility diameter of 40 nm.

3. Results and discussion

This technical note aims to experimentally determine the deposition of Soot- and Cu-UFP in an ALI cell exposure systems and compare the results with common theoretical deposition models. Three particle-associated PAH with ≥5 aromatic rings (Benzofluoranthenes [sum of b + j + k isomers], Benzo[e]pyrene and Benzo[a]pyrene) were targeted and quantified to use them as markers for the Soot-UFP. Copper was quantified from the ALI inserts for measuring the Cu-UFP.

3.1. UFP characterization

To understand the particle deposition in the Vitrocell® AES, the physical characteristics (GMD_{mob} and mass concentration) of the two UFP, comprising the Soot-UFP and Cu-UFP, were adjusted as similarly as possible.

Fig. 3 presents the number and mass size distributions of Soot-UFP and Cu-UFP. The geometric mean mobility diameters (GMD_{mob}) were 39 ± 3 nm for Soot-UFP and 33 ± 2 nm for Cu-UFP, indicating slightly smaller particle sizes for Cu-UFP. However, the particle number concentration of Cu-UFP was approximately twice as high as that of Soot-UFP. The primary particle size of Cu-UFP, generated via spark discharge, typically ranges from 1 to 9 nm (Roth et al., 2004), which is significantly smaller than that of Soot-UFP from the miniCAST soot generator (Das et al., 2024). We optimized the SDG settings to achieve a mobility diameter comparable to that of Soot-UFP, increasing its frequency to the maximum while using a 5 L vessel and a 3 m-long PFA coil with an internal diameter of 10 mm. Despite differences in number concentration, the mass concentration of both UFP remained similar, at approximately 90 µg m^{-3}.
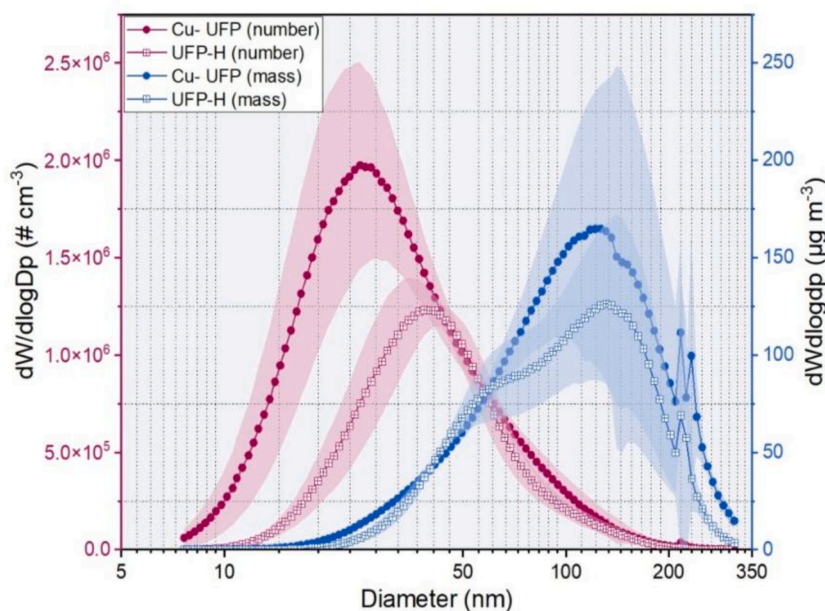

Fig. 3. Size distribution of Soot-UFP and Cu-UFP. The left y-axis shows the number size distribution (# cm^{-3}), while the right y-axis represents the mass size distribution (µg m^{-3}). Shaded areas indicate the standard deviation for each corresponding size bin.

Offline chemical characterization was performed on particle phase samples using QFF. For Soot-UFP, PAH were quantified by direct thermal desorption hyphenated gas chromatography-mass spectrometry (DTD-GCMS). The concentration of the PAH in the QFF samples is presented in Table 1. All PAH measured had similar concentrations of approximately 70 ng m^{-3}.

Cu-UFP samples collected on QFF were analyzed for Cu mass concentration quantification. The filter samples were analyzed using Atomic Absorption Spectroscopy (AAS), yielding a copper concentration of 80 µg m^{-3} ± 10 µg m^{-3} across all experiments (n = 5).

3.2. Measured mass deposition of the two UFP in the ALI

EMFAB filters for Soot-UFP and the empty inserts for Cu-UFP were used and exposed in the exposure units in two aerosol modules at the AES. Concurrently with ALI exposure in the AES, particulate-phase filter samples were collected on QFF outside the AES to monitor PAH concentrations. Fig. 4 illustrates the deposition of PAH per filter area for each exposed insert. Although the figures show differences in the determination of PAH from the respective inserts, statistical analysis using Welch's ANOVA revealed no significant differences in individual PAH levels between inserts (p > 0.05). This may be due to the smaller sample size and high variation between experiments at the AES. Additionally, Pearson correlation-based pattern analysis assessed potential variations in PAH composition across inserts, yielding a correlation value of 0.92 as the lowest. This strong correlation suggests a consistent distribution of PAH across all inserts, indicating no alteration of the PAH profile in the ALI system and confirming the reliability of the analytical quantification. Using the PAH markers, the mass deposition of the Soot-UFP was calculated and is represented in Table 2.

The deposition of Cu-UFP on inserts was conducted in four exposure units of the exposure module X (X1, X2, X3, X4) and five exposure units in the exposure module Y (Y1, Y2, Y3, Y5, Y6) in the VITROCELL® AES. Fig. 5 presents the measured Cu-UFP deposited in each exposed insert in the AES at the ALI. Similar to the Soot-UFP analysis, a Welch ANOVA was performed for Cu-UFP, revealing no significant differences between inserts (p > 0.05).

We observed that deposition variability differed across inserts, with lower relative variability at positions with low deposition (RSD ≈ 7 %, e.g., for X2) and higher variability at positions with high deposition (RSD ≈ 44 %, e.g., for Y6) for Cu-UFP. And the RSD deviated from 16 % for Y6 to 60 % for Y2 for Soot-UFP. This non-uniformity likely reflects local flow heterogeneity within the exposure module, combined with particle dynamics and analytical variability at higher deposited mass. Such variability has been previously reported for ALI systems, underscoring the importance of position-specific deposition measurements for accurate dose interpretation (Oldham et al., 2020). One limitation of this manuscript is the reasonable number of replicates for proper statistics on the individual insert variability and deposition uniformity was unfortunately not possible.

3.3. Comparison of measured and modelled deposition of UFP mass

For the theoretical estimation of deposition, the insert surface area of 4.67 cm^2 was used. Aerosol flow and temperature at each position were 100 mL min^{-1} and 37 °C, respectively. Equation (1) was used to calculate the modelled mass deposition of UFP, while Equation (2) was used to determine the deposition efficiency.

In the first approach, following the suggestion of Lucci et al. (2018), the aerosol boundary layer thickness was calculated using Equation (3). The effective density for Soot-UFP was estimated as 1g cm^{-3} based on previous measurements of CAST-burner-generated soot densities. Although fresh soot aggregate effective densities decrease strongly as a function of particle size, the smallest measured soot particles typically have densities close to unity (Leskinen et al., 2023). The effective density for Cu-UFP was estimated as 0.9 g cm^{-3} based on the copper agglomerate particle effective density function presented by Charvet et al. (2014) and by using the measured GMD of copper particles (33 nm). The selected density affects the calculations in two ways: first, by influencing the estimation of deposition efficiency, and more importantly, by converting the number of deposited particles into the corresponding deposited mass. This yielded a deposited mass area of 1.0 ± 0.2 ng cm^{-2} for Soot-UFP and 1.3 ± 0.2 ng cm^{-2} for Cu-UFP. For Soot-UFP, the model substantially underestimates the deposited Soot-UFP compared to experimental values. Specifically, the deposited mass of benzo-fluoranthenes [sum of b + j + k isomers], benz[a]pyrene, and benz[e]pyrene was found to be 7 to 8 times higher in the measurements than in the model predictions. Accordingly, the measured deposition efficiency for Soot-UFP was calculated to be 0.22 % ± 0.03 %. This deposition is similar to that observed by Bitterle et al. (2006) for carbonaceous UFP produced by a spark discharge generator. A similar trend was observed for Cu-UFP, where the model underestimated deposition by a factor of 5. The corresponding experimental deposition efficiency was 0.8 % ± 0.1 %.

The second approach defined the boundary layer thickness using Equation (4). This resulted in higher estimated UFP mass deposition, improving the alignment between model predictions and experimental data. The deposited mass area was calculated to be 3.1 ± 0.4 ng cm^{-2} for Soot-UFP and 3.8 ± 0.4 ng cm^{-2} for Cu-UFP. With this adjustment, the model underestimated Soot-UFP deposition by 2–3 times (instead of 7–8 times), and Cu-UFP deposition by a factor of 2 (rather than 5 times). The recalculated deposition efficiencies were 1 % for Soot-UFP and 2 % for Cu-UFP, aligning more closely with values reported in previous studies (Bitterle et al., 2006; Grabinski et al., 2015).

Table 1
The concentration of PAH acquired from DTD-GCMS from the particulate phase in Soot-UFP. The results indicate the concentration of each PAH ± standard deviation (n = 6).

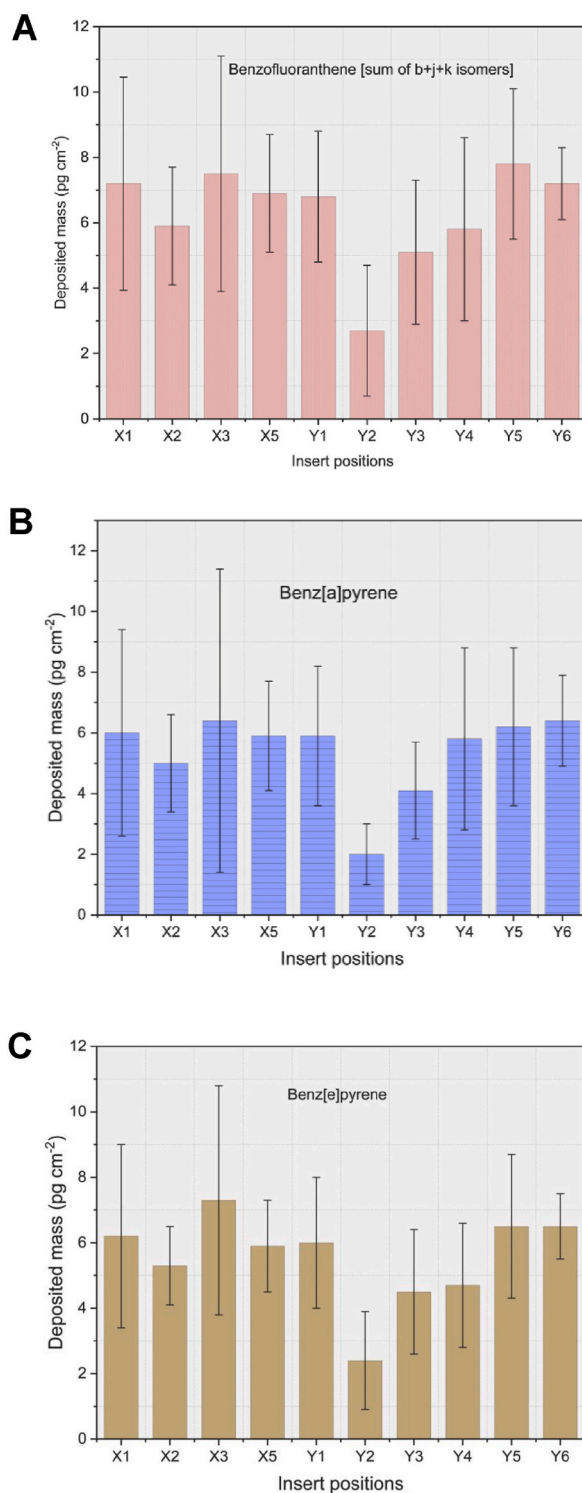| Benzofluoranthenes [sum of b + j + k isomers] (ng m^{-3})	Benzo[e]pyrene (ng m^{-3})	Benzo[a]pyrene (ng m^{-3})
70 ± 4	66 ± 5	71 ± 7

Fig. 4. Deposited mass of Soot-UFP quantified at different positions within the AES for selected PAH markers (N = 4): (A) Benzofluoranthene [sum of b + j + k isomers], (B) Benzo[a]pyrene, (C) Benzo[e]pyrene. The error bars represent the standard deviation of each targeted PAH at each position across all experiments. The relative standard deviation (RSD) ranged from 15 % (Y6) to 47 % (X3) for (A), from 24 % (Y6) to 78 % (X3) for (B), and from 16 % (Y6) to 60 % (Y2) for (C).

Table 2

The mass deposition of Soot-UFP in the X and Y units of the exposure system. The results indicate the Soot-UFP mass deposition± standard deviation (n = 6).

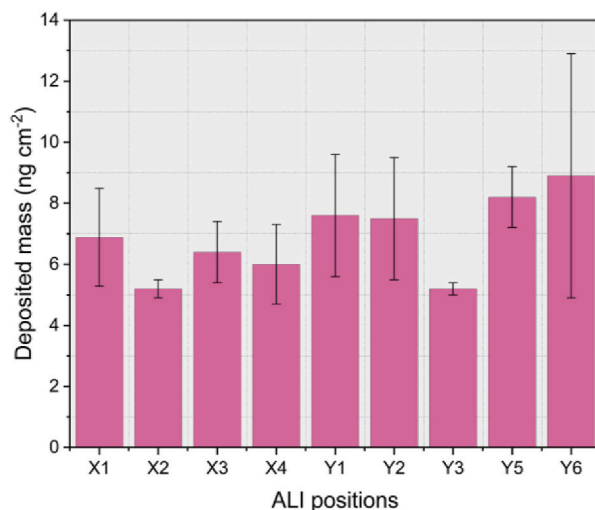| PAH	Soot-UFP Mass deposition From Unit X (ng cm^{-2})	Soot-UFP Mass deposition From Unit Y (ng cm^{-2})	Average Soot-UFP Mass deposition (ng cm^{-2})
Benzofluoranthenes[sum of b + j + k isomers]	9.0 ± 1.0	8.0 ± 1.0	8.4 ± 1.0
Benzo[e]pyrene	8.5 ± 1.0	7.6 ± 1.0	8.0 ± 1.0
Benzo[a]pyrene	7.3 ± 1.0	7.0 ± 1.0	7.1 ± 1.0

Fig. 5. Deposited mass of Cu-UFP quantified at different positions within the AES (N = 4). The error bars represent the standard deviation of copper mass quantified at each position across all experiments. The relative standard deviation (RSD) for Cu-UFP ranged from 7 % (X2) to 44 % (Y6).

Table 3

Comparison of the deposited mass of Soot-UFP and Cu-UFP mass deposition between the theoretical and experimental approaches in the experiments. The results are shown as the averages ± standard deviation of all the inserts.

Soot-UFP	Theoretical method (ng cm^{-2})		Experimental method (N = 5) (ng cm^{-2})		
	Lucci et al. (2018)	Grabinski et al. (2015)	Marker: Benzofluoranthene [sum of b + j + k isomers]	Marker: Benzo[a] pyrene	Marker: Benzo[e] pyrene
Experiment 1	1.1	3.3	9.1 ± 1.0	7.7 ± 1.0	8.6 ± 1.0
Experiment 2	0.8	2.2	8.1 ± 1.0	6.5 ± 1.0	7.5 ± 1.0
Experiment 3	1.2	3.5	8.8 ± 1.0	7.8 ± 1.0	8.5 ± 1.0
Experiment 4	0.9	2.7	7.0 ± 1.0	5.7 ± 1.0	6.6 ± 1.0
Experiment 5	1.1	3.2	8.9 ± 1.0	7.9 ± 1.0	8.5 ± 1.0
Cu-UFP	Theoretical method (ng cm^{-2})			Experimental method (N = 4) (ng cm^{-2})	
	Lucci et al. (2018)		Grabinski et al., 2015		
Experiment 1	1.4		4.1	7.0 ± 2.0	
Experiment 2	1.4		4.2	6.0 ± 1.0	
Experiment 3	1.4		4.2	6.7 ± 1.0	
Experiment 4	1.0		2.8	7.4 ± 1.0	

Using the experimental determined deposition (Table 3), the deposition efficiency increases to 1.2 % to 2 % for soot-UFP and 0.97–1.4 % for Cu-UFP, which is in agreement with a study with NaCl/fluorescein particles of a deposition efficiency of 1.6 % at similar ALI conditions (Mülhopt et l., 2016).

Our findings indicate that the modelled UFP mass deposition from both sources was consistently lower than the experimentally measured deposition in the investigated VITROCELL® AES (Table 3). It is essential to note that the theoretical model (Lucci et al., 2018) was initially developed for the VITROCELL® VC24/48 and AMES systems, utilizing a flow rate of 20 mL min^{-1}. In contrast, our study employed a higher flow rate of 100 mL min^{-1} with a fundamentally different aerosol exposure system. The sample extraction

from VITROCELL® VC24/48 and AMES systems occurs vertically without the use of a sampling probe or adherence to isokinetic sampling criteria, which results in the aerosol likely being drawn from the periphery rather than the core of the main flow. In comparison, the AES employs isokinetic sampling from the main flow. This approach is expected to yield more accurate and reproducible aerosol collection, and consequently, higher particle deposition. Although this was accounted for in the model, discrepancies between predicted and measured values remained. Notably, applying the boundary layer thickness approach from Hinds., (1999)Equation (4) improved the agreement with measured values compared to the approach by Lucci et al. (2018). Although Equation (4) was acknowledged by Lucci et al. (2018), it was not implemented in practice.

The used boundary layer thickness model affects the deposition efficiency of Brownian diffusion-driven particles, particularly. The efficiency ratio between the models is shown in Fig. 6. The ratio between the models is approximately 3 for particles with diameters of 80–200 nm, when both diffusion and settling mechanisms are included. As most of the particle mass in this study is within that range, the outcome is that the difference between the models is a factor of 3. The ratio between the models reaches the maximum at approximately 100 nm. This is because the factor of $2/3(v/D)^{(1/6)}$ increases with particle size as the diffusion coefficient decreases; however, for larger particles (>200 nm), settling starts to take a dominant role in deposition.

Deposition prediction in the diffusion regime remains challenging when using ALI systems. While theoretical modeling is a valuable tool, experimental validation is crucial, as slight variations can significantly impact the results, especially in toxicological assessments. The unknown variability in particle deposition between inserts and non-uniform deposition within inserts can introduce uncontrolled differences in the delivered dose, making it challenging to compare biological responses across replicates. This undermines dose–response assessment and increases the risk of attributing observed cellular effects to exposure artifacts. Especially for UFP, the deposition efficiency calculations must be taken with care. We focused on mass deposition in this study; however, these discrepancies will be enhanced if the number deposition efficiencies of UFP are discussed in relation to biological interactions.

4. Conclusion

Determining mass deposition in air-liquid interface (ALI) exposure systems, such as the VITROCELL® AES, is complex when dealing with ultrafine particles (UFP) due to their small size and dynamic behavior. This study quantified the deposition of Soot-UFP and Cu-UFP using specific methods: thermal desorption gas chromatography-mass spectrometry (TD-GCMS) for soot-UFP, analyzed through polycyclic aromatic hydrocarbon (PAH) markers, and atomic absorption spectroscopy (AAS) for copper UFP. For Soot-UFP, the deposition efficiencies were approximately 0.22 %, whereas for Cu-UFP, they were 0.8 %. The experimental deposition efficiencies exceeded estimates by a factor of 8 for Soot-UFP and 5 for Cu-UFP when compared to the theoretical model presented by Lucci et al. (2018). This discrepancy is likely due to assumptions about boundary layer thickness and particle flux that were based on different ALI system designs and sampling setups. However, we were able to reduce the underestimation to factors of 2–3 for Soot-UFP and 2 for copper UFP by using an updated model that takes Brownian displacement into account when estimating boundary layer thickness unique to the AES system. These findings underscore the crucial need for system-specific adjustments in deposition models to account for flow dynamics, sampling rates, and aerosol properties. From a biological perspective, accurate deposition assessment is essential because the delivered particle dose directly determines the magnitude of cellular responses. Underestimating deposition may lead to an apparent amplification of toxicity per unit mass, whereas overestimation could mask true biological effects. The improved deposition modeling presented here therefore not only advances the physical understanding of aerosol behavior in ALI systems, but also strengthens the reliability of dose–response relationships in toxicological studies. This is particularly critical for ultrafine particles, whose high surface area and reactivity can trigger disproportionate cellular responses even at low mass doses. By refining deposition estimates, we enable more meaningful interpretation of *in vitro* data and improve their relevance for human health risk assessment.

CRediT authorship contribution statement

Anusmita Das: Writing – review & editing, Writing – original draft, Visualization, Validation, Methodology, Investigation, Formal analysis, Data curation, Conceptualization. **Mathilde Noemie Delaval:** Writing – review & editing, Validation, Supervision, Project administration, Methodology, Investigation, Funding acquisition, Data curation, Conceptualization. **Mika Ihalainen:** Writing – review & editing, Validation, Methodology, Investigation. **Jürgen Schnelle-Kreis:** Writing – review & editing, Supervision, Resources, Project administration, Funding acquisition, Data curation, Conceptualization. **Anja Huber:** Investigation. **Elias J. Zimmermann:** Writing – review & editing, Methodology, Investigation. **Sebastiano Di Bucchianico:** Writing – review & editing, Project administration, Funding acquisition. **Olli Sippula:** Writing – review & editing, Supervision, Resources. **Hendryk Czech:** Writing – review & editing, Supervision, Formal analysis. **Martin Sklorz:** Writing – review & editing, Supervision, Resources, Methodology, Investigation, Funding acquisition, Conceptualization. **Ralf Zimmermann:** Writing – review & editing, Supervision, Resources.
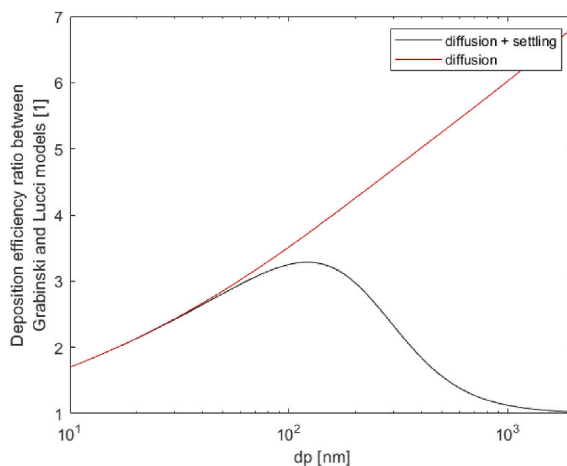
Funding sources

Fig. 6. The ratio of deposition efficiency calculated with the boundary layer thickness model used in Grabinski et al., 2015 to deposition efficiency calculated with the boundary layer thickness model used in Lucci et al., 2018. The ratio is illustrated in two cases: one where the only deposition mechanism is diffusion, and another where settling is also considered. The flow rate is 100 mL min^{-1} and the particle effective density is 1000 kg m^{-3}.

Declaration of competing interest

The authors declare that they have no known competing financial interests or personal relationships that could have appeared to influence the work reported in this paper.

Data availability

Data will be made available on request.

References

Adamson, J., Thorne, D., McAughey, J., Dillon, D., & Meredith, C. (2013). Quantification of cigarette smoke particle deposition in vitro using a triplicate quartz crystal microbalance exposure chamber. *BioMed Research International, 2013*, 685074. https://doi.org/10.1155/2013/685074

Adamson, J., Thorne, D., Zainuddin, B., Baxter, A., McAughey, J., & Gaça, M. (2016). Application of dosimetry tools for the assessment of e-cigarette aerosol and cigarette smoke generated on two different in vitro exposure systems. *Chemistry Central Journal, 10*, 74. https://doi.org/10.1186/s13065-016-0221-9

Aufderheide, M., Heller, W.-D., Krischenowski, O., Möhle, N., & Hochrainer, D. (2017). Improvement of the CULTEX® exposure technology by radial distribution of the test aerosol. *Experimental & Toxicologic Pathology, 69*, 359–365. https://doi.org/10.1016/j.etp.2017.02.004

Bannuscher, A., Schmid, O., Drasler, B., Rohrbasser, A., Braakhuis, H. M., Meldrum, K., Zwart, E. P., Gremmer, E. R., Birk, B., Rissel, M., Landsiedel, R., Moschini, E., Evans, S. J., Kumar, P., Orak, S., Doryab, A., Erdem, J. S., Serchi, T., Vandebriel, R. J., … Rothen-Rutishauser, B. (2022). An inter-laboratory effort to harmonize the cell-delivered in vitro dose of aerosolized materials. *NanoImpact, 28*, 100439. https://doi.org/10.1016/j.impact.2022.100439

Binder, S., Rastak, N., Karg, E., Huber, A., Kuhn, E., Dragan, G. C., Monsé, C., Breuer, D., Di Bucchianico, S., Delaval, M. N., Oeder, S., Sklorz, M., & Zimmermann, R. (2022). Construction of an in vitro air–liquid interface exposure system to assess the toxicological impact of gas and particle phase of semi-volatile organic compounds. *Toxics, 10*. https://doi.org/10.3390/toxics10120730

Bitterle, E., Karg, E., Schroeppel, A., Kreyling, W. G., Tippe, A., Ferron, G. A., Schmid, O., Heyder, J., Maier, K. L., & Hofer, T. (2006). Dose-controlled exposure of A549 epithelial cells at the air–liquid interface to airborne ultrafine carbonaceous particles. *Chemosphere, 65*, 1784–1790. https://doi.org/10.1016/j.chemosphere.2006.04.035

Charvet, A., Bau, S., Paez Coy, N. E., Bémer, D., & Thomas, D. (2014). Characterizing the effective density and primary particle diameter of airborne nanoparticles produced by spark discharge using mobility and mass measurements (tandem DMA/APM). *Journal of Nanoparticle Research, 16*, 2418. https://doi.org/10.1007/s11051-014-2418-y

Comouth, A., Saathoff, H., Naumann, K.-H., Muelhopt, S., Paur, H.-R., & Leisner, T. (2013). Modelling and measurement of particle deposition for cell exposure at the air–liquid interface. *Journal of Aerosol Science, 63*, 103–114. https://doi.org/10.1016/j.jaerosci.2013.04.009

Das, A., Pantzke, J., Jeong, S., Hartner, E., Zimmermann, E. J., Gawlitta, N., Offer, S., Shukla, D., Huber, A., Rastak, N., Meščeriakovas, A., Ivleva, N. P., Kuhn, E., Binder, S., Gröger, T., Oeder, S., Delaval, M., Czech, H., Sippula, O., … Zimmermann, R. (2024). Generation, characterization, and toxicological assessment of reference ultrafine soot particles with different organic content for inhalation toxicological studies. *Science of the Total Environment, 951*, Article 175727. https://doi.org/10.1016/j.scitotenv.2024.175727

Delaval, M. N., Jonsdottir, H. R., Leni, Z., Keller, A., Brem, B. T., Siegerist, F., Schönenberger, D., Durdina, L., Elser, M., Salathe, M., Baumlin, N., Lobo, P., Burtscher, H., Liati, A., & Geiser, M. (2022). Responses of reconstituted human bronchial epithelia from normal and health-compromised donors to non-volatile particulate matter emissions from an aircraft turbofan engine. *Environmental Pollution, 307*, Article 119521. https://doi.org/10.1016/j.envpol.2022.119521

Folwarczny, E., Forster, F., Jörres, R. A., Rakete, S., Ye, S., Wenig, M., Gawlitta, N., Schnelle-Kreis, J., Winterhalter, R., Müller, A., Nowak, D., & Karrasch, S. (2025). Acute health effects of ambient air pollution including ultrafine particles in a semi-experimental setting in young, healthy individuals. *Particle and Fibre Toxicology, 22*, 14. https://doi.org/10.1186/s12989-025-00628-7

Font, O., Moreno, T., Querol, X., Martins, V., Sánchez Rodas, D., de Miguel, E., & Capdevila, M. (2019). Origin and speciation of major and trace PM elements in the Barcelona subway system. *Transportation Research Part Transp. Environ., 72*, 17–35. https://doi.org/10.1016/j.trd.2019.03.007

Fujitani, Y., Sugaya, Y., Hashiguchi, M., Furuyama, A., Hirano, S., & Takami, A. (2015). Particle deposition efficiency at air–liquid interface of a cell exposure chamber. *Journal of Aerosol Science, 81*, 90–99. https://doi.org/10.1016/j.jaerosci.2014.10.012

Fussell, J. C., Franklin, M., Green, D. C., Gustafsson, M., Harrison, R. M., Hicks, W., Kelly, F. J., Kishta, F., Miller, M. R., Mudway, I. S., Oroumiyeh, F., Selley, L., Wang, M., & Zhu, Y. (2022). A review of road traffic-derived non-exhaust particles: Emissions, physicochemical characteristics, health risks, and mitigation measures. *Environmental Science and Technology, 56*, 6813–6835. https://doi.org/10.1021/acs.est.2c01072

Grabinski, C. M., Hussain, S. M., & Mohan Sankaran, R. (2015). Simulations of submicron aerosol deposition at an air–liquid interface for in vitro toxicology. *Journal of Aerosol Science, 90*, 87–102. https://doi.org/10.1016/j.jaerosci.2015.08.005

Hakkarainen, H., Järvinen, A., Lepistö, T., Salo, L., Kuittinen, N., Laakkonen, E., Yang, M., Martikainen, M.-V., Saarikoski, S., Aurela, M., Barreira, L., Teinilä, K., Ihalainen, M., Aakko-Saksa, P., Timonen, H., Rönkkö, T., & Jalava, P. (2023). Toxicity of exhaust emissions from high aromatic and non-aromatic diesel fuels using in vitro ALI exposure system. *Science of the Total Environment, 890*, Article 164215. https://doi.org/10.1016/j.scitotenv.2023.164215

Hinds, W. C. (1999). *Aerosol technology: Properties, behavior, and measurement of airborne particles* (second). Wiley.

Hofmann, W. (2011). Modelling inhaled particle deposition in the human lung—A review. *Journal of Aerosol Science, 42*, 693–724. https://doi.org/10.1016/j.jaerosci.2011.05.007

Jonsdottir, H. R., Delaval, M., Leni, Z., Keller, A., Brem, B. T., Siegerist, F., Schönenberger, D., Durdina, L., Elser, M., Burtscher, H., Liati, A., & Geiser, M. (2019). Non-volatile particle emissions from aircraft turbine engines at ground-idle induce oxidative stress in bronchial cells. *Communications Biology, 2*, 90. https://doi.org/10.1038/s42003-019-0332-7

Juarez Facio, A. T., Yon, J., Corbière, C., Rogez-Florent, T., Castilla, C., Lavanant, H., Mignot, M., Devouge-Boyer, C., Logie, C., Chevalier, L., Vaugeois, J.-M., & Monteil, C. (2022). Toxicological impact of organic ultrafine particles (UFPs) in human bronchial epithelial BEAS-2B cells at air-liquid interface. *Toxicology in Vitro, 78*, Article 105258.

Karg, E. W., Ferron, G. A., Bauer, S., Di Bucchianico, S., & Zimmermann, R. (2020). Is the particle deposition in a cell exposure facility comparable to the lungs? A computer model approach. *Aerosol Science & Technology, 54*, 668–684. https://doi.org/10.1080/02786826.2020.1724868

Kim, J. S., Peters, T. M., O'Shaughnessy, P. T., Adamcakova-Dodd, A., & Thorne, P. S. (2013). Validation of an in vitro exposure system for toxicity assessment of air-delivered nanomaterials. *Toxicology in Vitro, 27*, 164–173. https://doi.org/10.1016/j.tiv.2012.08.030

Kim, B., Shin, J. H., Kim, H. P., Jo, M. S., Kim, H. S., Lee, J. S., Lee, H. K., Kwon, H. C., Han, S. G., Kang, N., Gulumian, M., Bello, D., & Yu, I. J. (2022). On-Site deployment of an air-liquid-interphase device to assess health hazard potency of airborne workplace contaminants: The case of 3-D printers. *Frontier Toxicology, 4*.

Kwon, H.-S., Ryu, M. H., & Carlsten, C. (2020). Ultrafine particles: Unique physicochemical properties relevant to health and disease. *Experimental and Molecular Medicine, 52*, 318–328. https://doi.org/10.1038/s12276-020-0405-1

Leskinen, J., Hartikainen, A., Väätäinen, S., Ihalainen, M., Virkkula, A., Mesceriakovas, A., Tiitta, P., Miettinen, M., Lamberg, H., Czech, H., Yli-Pirilä, P., Tissari, J., Jakobi, G., Zimmermann, R., & Sippula, O. (2023). Photochemical aging induces changes in the effective densities, morphologies, and optical properties of combustion aerosol particles. *Environmental Science and Technology, 57*, 5137–5148. https://doi.org/10.1021/acs.est.2c04151

Liu, X., Deming, B., Pagonis, D., Day, D. A., Palm, B. B., Talukdar, R., Roberts, J. M., Veres, P. R., Krechmer, J. E., Thornton, J. A., de Gouw, J. A., Ziemann, P. J., & Jimenez, J. L. (2019). Effects of gas–wall interactions on measurements of semivolatile compounds and small polar molecules. *Atmospheric Measurement Techniques, 12*, 3137–3149. https://doi.org/10.5194/amt-12-3137-2019

Lucci, F., Castro, N. D., Rostami, A. A., Oldham, M. J., Hoeng, J., Pithawalla, Y. B., & Kuczaj, A. K. (2018). Characterization and modeling of aerosol deposition in vitrocell® exposure systems - Exposure well chamber deposition efficiency. *Journal of Aerosol Science, 123*, 141–160. https://doi.org/10.1016/j.jaerosci.2018.06.015

Moreno-Ríos, A. L., Tejeda-Benítez, L. P., & Bustillo-Lecompte, C. F. (2022). Sources, characteristics, toxicity, and control of ultrafine particles: An overview. *Geoscience Frontiers, 13*, Article 101147. https://doi.org/10.1016/j.gsf.2021.101147

Mülhopt, S., Dilger, M., Diabaté, S., Schlager, C., Krebs, T., Zimmermann, R., Buters, J., Oeder, S., Wäscher, T., Weiss, C., & Paur, H.-R. (2016). Toxicity testing of combustion aerosols at the air–liquid interface with a self-contained and easy-to-use exposure system. *Journal of Aerosol Science, 96*, 38–55. https://doi.org/10.1016/j.jaerosci.2016.02.005

Neilson, L., Mankus, C., Thorne, D., Jackson, G., DeBay, J., & Meredith, C. (2015). Development of an in vitro cytotoxicity model for aerosol exposure using 3D reconstructed human airway tissue; application for assessment of e-cigarette aerosol. *Toxicology in Vitro, 29*, 1952–1962. https://doi.org/10.1016/j.tiv.2015.05.018

Neukirchen, C., Saraji-Bozorgzad, M. R., Mäder, M., Mudan, A. P., Czasch, P., Becker, J., Di Bucchianico, S., Trapp, C., Zimmermann, R., & Adam, T. (2025). Comprehensive elemental and physical characterization of vehicle brake wear emissions from two different brake pads following the global technical regulation methodology. *The Journal of Hazardous Materials, 482*, Article 136609. https://doi.org/10.1016/j.jhazmat.2024.136609

Offer, S., Hartner, E., Di Bucchianico, S., Bisig, C., Bauer, S., Pantzke, J., … Zimmermann, R. (2022). Effect of atmospheric aging on soot particle toxicity in lung cell models at the air–liquid interface: Differential toxicological impacts of biogenic and anthropogenic secondary organic aerosols (SOAs). *Environmental Health Perspectives, 130*, 27003–27021. https://doi.org/10.1289/EHP9413

Ohlwein, S., Kappeler, R., Kutlar Joss, M., Künzli, N., & Hoffmann, B. (2019). Health effects of ultrafine particles: A systematic literature review update of epidemiological evidence. *International Journal of Public Health, 64*, 547–559. https://doi.org/10.1007/s00038-019-01202-7

Oldham, M. J., Castro, N., Zhang, J., Rostami, A., Lucci, F., Pithawalla, Y., Kuczaj, A. K., Gilman, I. G., Pasha, K., Julia, H., & Lee, K. M. (2020). Deposition efficiency and uniformity of monodisperse solid particle deposition in the vitrocell® 24/48 Air–liquid-interface in vitro exposure system. *Aerosol Science & Technology, 54*, 52–65. https://doi.org/10.1080/02786826.2019.1676877

Orasche, J., Schnelle-Kreis, J., Abbaszade, G., & Zimmermann, R. (2011). Technical note: In-situ derivatization thermal desorption GC-TOFMS for direct analysis of particle-bound non-polar and polar organic species. *Atmospheric Chemistry and Physics, 11*, 8977–8993. https://doi.org/10.5194/acp-11-8977-2011

Pantzke, J., Koch, A., Zimmermann, E. J., Rastak, N., Offer, S., Bisig, C., Bauer, S., Oeder, S., Orasche, J., Fiala, P., Stintz, M., Rüger, C. P., Streibel, T., Di Bucchianico, S., & Zimmermann, R. (2023). Processing of carbon-reinforced construction materials releases PM2.5 inducing inflammation and (secondary) genotoxicity in human lung epithelial cells and fibroblasts. *Environmental Toxicology and Pharmacology, 98*, Article 104079. https://doi.org/10.1016/j.etap.2023.104079

Pardo, M., Czech, H., Offer, S., Sklorz, M., Di Bucchianico, S., Hartner, E., Pantzke, J., Kuhn, E., Paul, A., Ziehm, T., Zhang, Z.-H., Jakobi, G., Bauer, S., Huber, A., Zimmermann, J., Rastak, N., Binder, S., Brejcha, R., Schneider, E., … Rudich, Y. (2023). Atmospheric aging increases the cytotoxicity of bare soot particles in BEAS-2B lung cells. *Aerosol Science & Technology, 57*, 367–383. https://doi.org/10.1080/02786826.2023.2178878

Paur, H.-R., Cassee, F. R., Teeguarden, J., Fissan, H., Diabate, S., Aufderheide, M., Kreyling, W. G., Hänninen, O., Kasper, G., Riediker, M., Rothen-Rutishauser, B., & Schmid, O. (2011). In-vitro cell exposure studies for the assessment of nanoparticle toxicity in the lung—A dialog between aerosol science and biology. *Journal of Aerosol Science, 42*, 668–692. https://doi.org/10.1016/j.jaerosci.2011.06.005

Roth, C., Ferron, G. A., Karg, E., Lentner, B., Schumann, G., Takenaka, S., & Heyder, J. (2004). Generation of ultrafine particles by spark discharging. *Aerosol Science & Technology, 38*, 228–235. https://doi.org/10.1080/02786820490247632

Schnelle-Kreis, J., Welthagen, W., Sklorz, M., & Zimmermann, R. (2005). Application of direct thermal desorption gas chromatography and comprehensive two-dimensional gas chromatography coupled to time of flight mass spectrometry for analysis of organic compounds in ambient aerosol particles. *Journal of Separation Science, 28*, 1648–1657. https://doi.org/10.1002/jssc.200500120

Schraufnagel, D. E. (2020). The health effects of ultrafine particles. *Experimental and Molecular Medicine, 52*, 311–317. https://doi.org/10.1038/s12276-020-0403-3

Schwarz, M., Schneider, A., Cyrys, J., Bastian, S., Breitner, S., & Peters, A. (2023). Impact of ambient ultrafine particles on cause-specific mortality in three German cities. *American Journal of Respiratory and Critical Care Medicine, 207*, 1334–1344. https://doi.org/10.1164/rccm.202209-1837OC

Steiner, S., Majeed, S., Kratzer, G., Vuillaume, G., Hoeng, J., & Frentzel, S. (2017). Characterization of the vitrocell® 24/48 aerosol exposure system for its use in exposures to liquid aerosols. *Toxicology in Vitro, 42*, 263–272. https://doi.org/10.1016/j.tiv.2017.04.021

Thorne, D., & Adamson, J. (2013). A review of in vitro cigarette smoke exposure systems. *Experimental & Toxicologic Pathology, 65*, 1183–1193. https://doi.org/10.1016/j.etp.2013.06.001

Tippe, A., Heinzmann, U., & Roth, C. (2002). Deposition of fine and ultrafine aerosol particles during exposure at the air/cell interface. *Journal of Aerosol Science, 33*, 207–218. https://doi.org/10.1016/S0021-8502(01)00158-6

Vallabani, N. V. S., Gruzieva, O., Elihn, K., Juárez-Facio, A. T., Steimer, S. S., Kuhn, J., Silvergren, S., Portugal, J., Piña, B., Olofsson, U., Johansson, C., & Karlsson, H. L. (2023). Toxicity and health effects of ultrafine particles: Towards an understanding of the relative impacts of different transport modes. *Environmental Research, 231*, Article 116186. https://doi.org/10.1016/j.envres.2023.116186

Zimmermann, E. J., Das, A., Huber, A., Gawlitta, N., Kuhn, E., Schlager, C., Gutmann, B., Krebs, T., Schnelle-Kreis, J., Delaval, M. N., & Zimmermann, R. (2025). Toxicological effects of long-term continuous exposure to ambient air on human bronchial epithelial Calu-3 cells exposed at the air-liquid interface. *Environmental Research, 269*, Article 120759. https://doi.org/10.1016/j.envres.2025.120759